Bulletin of Mathematical Biology (2007) 69: 2199–2225
DOI 10.1007/s11538-007-9213-1

ORIGINAL ARTICLE

Soft Tissue Modelling of Cardiac Fibres for Use in Coupled Mechano-Electric Simulations

Jonathan P. Whiteley*, Martin J. Bishop, David J. Gavaghan

Oxford University Computing Laboratory, Wolfson Building, Parks Road,
Oxford OX1 3QD, UK

Received: 14 March 2006 / Accepted: 7 March 2007 / Published online: 24 April 2007

Abstract The numerical solution of the coupled system of partial differential and ordinary differential equations that model the whole heart in three dimensions is a considerable computational challenge. As a consequence, it is not computationally practical—either in terms of memory or time—to repeat simulations on a finer computational mesh to ensure that convergence of the solution has been attained. In an attempt to avoid this problem while retaining mathematical rigour, we derive a one dimensional model of a cardiac fibre that takes account of elasticity properties in three structurally defined axes within the myocardial tissue. This model of a cardiac fibre is then coupled with an electrophysiological cell model and a model of cellular electromechanics to allow us to simulate the coupling of the electrical and mechanical activity of the heart. We demonstrate that currently used numerical methods for coupling electrical and mechanical activity do not work in this case, and identify appropriate numerical techniques that may be used when solving the governing equations. This allows us to perform a series of simulations that: (i) investigate the effect of some of the assumptions inherent in other models; and (ii) reproduce qualitatively some experimental observations.

Keywords Cardiac modelling · Electrophysiology · Soft tissue modelling

1. Introduction

The electrical activity of the heart generates an active tension that causes the heart to deform. It is therefore clearly evident that the mechanical activity of the heart is heavily dependent on the electrical activity. In turn, the mechanical activity affects the propagation of electrical activity, although this dependence is believed to be much weaker than the dependence in the opposite direction.

There is a substantial body of literature devoted to modelling the electrical activity of the heart, resulting in the development of a very large number of mathematical models. For a comprehensive selection of these models see, for example, the cellML website (cellML) or Nickerson (2004). Almost all of these models neglect the effect of mechanical contraction.

---

*Corresponding author.
E-mail address: Jonathan.Whiteley@comlab.ox.ac.uk (Jonathan P. Whiteley).

Any elasticity model of mechanical deformations requires a relationship between stress and strain. For cardiac tissue it has long been known that a nonlinear relationship between stress and strain is required to calculate accurate deformations (Janz et al., 1974). Two families of nonlinear relationships have been used: exponential relationships (Costa et al., 2001; Guccione et al., 1995; Janz et al., 1974); and pole–zero relationships (Hunter et al. 1997, 1998; Nash and Hunter, 2000). In this paper we focus on a pole–zero stress–strain relationship: similar results would be obtained with an exponential stress–strain relationship. A further requirement of a stress–strain relationship for cardiac tissue is that it enforces incompressibility of the tissue. This requirement has not always been enforced or, in some cases, has been enforced incorrectly. We discuss this further later on in this study.

Cardiac tissue consists of sheets of fibres stacked on top of each other. The more detailed stress–strain relationships that have been proposed (Costa et al., 2001; Guccione et al., 1995; Hunter et al. 1997, 1998; Nash and Hunter, 2000) take account of both fibre and sheet orientation in order to allow the tissue to have preferred directions for deformation. At each point within the tissue, a set of orthogonal, right-hand oriented axes is defined in which the first axis is along the cardiac fibre, the second axis is in the sheet of fibres and orthogonal to the first axis, and the third axis is orthogonal to the first two axes.

The governing equations for soft tissue deformations arise from Newton's second law, i.e. the net force acting is equal to the rate of change of momentum. All studies to date assume that the timescale on which the elastic force balances the active tension is negligible compared to other timescales in the problem. A consequence of this assumption is that the term that includes the second time derivative in the governing equations may be neglected. This is an attractive assumption from a computational viewpoint as the governing equations are elliptic instead of hyperbolic, and there is no need to address the stability issues associated with the solution of hyperbolic equations. This assumption has, to the best of our knowledge, never been validated for cardiac modelling.

In this study, we begin by writing down a soft tissue model of a cardiac fibre that includes all the features of the more detailed strain energy functions described above. The numerical solution of the coupled system of partial differential and ordinary differential equations that model the whole heart in three dimensions is a considerable computational challenge. Hunter et al. (2003) report that solving only the electrical activity requires "many days on a high-performance computer". As a consequence, it is not computationally practical—either in terms of memory or time—to repeat simulations on a finer computational mesh to confirm that the solution has indeed converged. To avoid this problem, we restrict ourselves to one spatial dimension. We use uniaxial tension to derive a stress–strain relationship for extension and compression of a cardiac fibre that takes account of differing elasticity properties in three orthogonal directions. This model of a cardiac fibre is then coupled with the electrophysiological model described by Noble et al. (1998) and a recently published model of cellular electromechanics (Niederer et al., 2006). We then investigate appropriate numerical methods for use when solving the coupled system of differential equations. First, we show that currently used numerical methods exhibit unstable behaviour, and identify a method that is stable. We use this stable numerical technique to perform numerical simulations. The first set of simulations investigate the effect of some of the assumptions inherent in other models. The second set of simulations match qualitatively some experimental observations.

2. The governing equations

Throughout this study we denote the coordinates of the undeformed, stress-free body by $\mathbf{X} = (X_1, X_2, X_3)^t$ and the coordinates of the deformed body by $\mathbf{x} = (x_1, x_2, x_3)^t$. The region occupied by the undeformed body is denoted by Ω_0, and the time period of interest is given by $t_0 < t < t_1$. We begin by describing separately mathematical models of the mechanical and electrical activity of the heart, and then describe a model that is used to couple these components via the generation of active tensions.

2.1. Soft tissue mechanics

2.1.1. The governing equations

The deformation gradient tensor F, the Cauchy–Green deformation tensor C, and the Lagrange–Green strain tensor E are defined by

$$F_{iM} = \frac{\partial x_i}{\partial X_M}, \qquad C = F^t F, \qquad E = \frac{1}{2}(C - I). \tag{1}$$

Note that we follow the convention of using lower case indices for quantities associated with the deformed body, and upper case indices for quantities associated with the undeformed body.

The second Piola–Kirchoff stress tensor T has entries T_{MN}, $M, N = 1, 2, 3$, that are defined to be the force per unit undeformed area acting on the undeformed body in the direction of X_M on a surface with normal in the X_N direction. As well as being dependent on the displacement, the entries of T are also functions of an unknown function $p(\mathbf{X})$ that is a Lagrange multiplier used to enforce incompressibility of cardiac tissue. Calculation of the entries of T in terms of the entries of E and p is discussed in Section 2.1.3.

The deformed coordinates satisfy, for $\mathbf{X} \in \Omega$ and $t_0 < t < t_1$, the hyperbolic partial differential equation (Makridakis, 1993):

$$\rho \frac{\partial^2 x_i}{\partial t^2} = \frac{\partial}{\partial X_M}\left(T_{MN} \frac{\partial x_i}{\partial X_N}\right), \quad i = 1, 2, 3, \tag{2}$$

$$\det(F) = 1, \tag{3}$$

where ρ is the density of the body. The boundary $\partial\Omega_0$ should be partitioned into two non-intersecting sets—one set $\partial\Omega_0^D$ where Dirichlet boundary conditions apply, and another set $\partial\Omega_0^N$ where Neumann boundary conditions apply. Boundary conditions are then given by

$$x_i(\mathbf{X}) = \hat{x}_i(\mathbf{X}), \quad \mathbf{X} \in \partial\Omega_0^D, \ i = 1, 2, 3,$$

$$T_{MN} \frac{\partial x_i}{\partial X_N} \nu_M = s_i(\mathbf{X}), \quad \mathbf{X} \in \partial\Omega_0^N, \ i = 1, 2, 3,$$

where, for $i = 1, 2, 3$, $\hat{x}_i$ and s_i are prescribed functions, and $\boldsymbol{\nu}$ is the outward pointing normal vector. Finally, initial conditions $\mathbf{x}(\mathbf{X}, t_0) = \mathbf{x}_0(\mathbf{X})$ should be specified.

As discussed in the Introduction, all previous work (Nash and Hunter, 2000; Nash and Panfilov, 2004) has made the assumption that the second time derivative on the left-hand side of (2) may be neglected. Note that (2) and (3) comprise four equations for four dependent functions x_1, x_2, x_3, p.

2.1.2. *Fibre orientation*

As discussed in the Introduction, realistic strain energy functions require the use of a right-hand coordinate system where, at each point of the tissue, the first axis is in the direction of the fibre, the second axis is in the plane of the fibre sheet and perpendicular to the first axis, and the third axis is perpendicular to the sheet of the fibre. Fibre direction varies throughout the heart, and so there is no fixed global coordinate system that satisfies these conditions. Instead, at each point of the tissue, we specify a rotation of the original, fixed axes that give a set of axes aligned with the fibre and the fibre sheet. Denoting a set of basis vectors for the axes aligned with the fibre and the fibre sheet by N_1^*, N_2^* and N_3^*, we may write the vector $\mathbf{X}$ in terms of this basis as

$$\mathbf{X} = X_1^* N_1^* + X_2^* N_2^* + X_3^* N_3^*.$$

An orthogonal matrix P that rotates axes aligned with the fibre and fibre sheet onto the original axes has entries

$$P_{MS} = \frac{\partial X_M}{\partial X_S^*}.$$

Using $P^t = P^{-1}$ allows us to interchange between tensors in the original frame and tensors in the fibre and fibre sheet oriented frame as follows:

$$E^* = P^t E P, \tag{4}$$

$$C^* = P^t C P, \tag{5}$$

$$T^* = P^t T P, \tag{6}$$

where we use the superscript * to denote a tensor with respect to axes aligned with the fibre and fibre sheet, and no superscript to denote the tensor with respect to the original axes.

2.1.3. *Calculating the entries of the second Piola–Kirchoff stress tensor*

The strain energy function, $W(\mathbf{X}, t)$, is defined to be the elastic energy per unit undeformed volume. We therefore have

$$\text{Elastic energy} = \int_{\Omega_0} W(\mathbf{X}, t)\, \mathrm{d}\mathbf{X}.$$

In this study we use the pole–zero strain energy function that has been used by other authors (Hunter et al. 1997, 1998; Nash and Hunter, 2000). This strain energy function is defined in terms of the strain tensor with respect to axes aligned with the fibre and the fibre sheet, and so we first use (4) to compute E^* from E. The strain energy function is then given by

$$\begin{aligned} W = {} & k_1 \frac{(E^*_{11_+})^2}{(a_1 - E^*_{11})^{b_1}} + k_2 \frac{(E^*_{22_+})^2}{(a_2 - E^*_{22})^{b_2}} + k_3 \frac{(E^*_{33_+})^2}{(a_3 - E^*_{33})^{b_3}} \\ & + k_4 \frac{(E^*_{12_+})^2}{(a_3 - E^*_{12})^{b_4}} + k_5 \frac{(E^*_{13_+})^2}{(a_5 - E^*_{13})^{b_5}} + k_6 \frac{(E^*_{23_+})^2}{(a_6 - E^*_{23})^{b_6}}, \end{aligned} \tag{7}$$

where we use the notation

$$E^*_{MN_+} = \begin{cases} E^*_{MN}, & E^*_{MN} \geq 0, \\ 0, & E^*_{MN} < 0. \end{cases}$$

The entries of T^* are given by

$$T^*_{MN} = \frac{1}{2}\left(\frac{\partial W}{\partial E^*_{MN}} + \frac{\partial W}{\partial E^*_{NM}}\right) - p(C^*)^{-1}_{MN} + T_a \delta_{M1}\delta_{N1}(C^*)^{-1}_{MN}, \tag{8}$$

where C^* is computed from C using (5). The first two terms on the right-hand side of the expression above for T^*_{MN} are the elastic forces arising, with the second of these terms enforcing incompressibility of the body. The final term includes the active tension T_a that is generated by the model that will be discussed in Section 2.3. Although the active tension has components that act in all spatial directions (Usyk et al., 2000) we use the common assumption that components orthogonal to the fibre direction may be neglected (Nash and Hunter, 2000; Remme et al., 2005; Smith et al., 2004). Finally, T can be computed from T^* using (6), allowing us to solve (2) and (3) to compute $\mathbf{x}$ and p.

2.2. *Cardiac electrophysiological models*

The general form of the monodomain equations that may be used to model the generation and propagation of electrical activity in the heart is given by (Keener and Sneyd, 1998):

$$\mathcal{C}\frac{\partial v_1}{\partial t} = \frac{1}{\chi}\frac{\partial}{\partial X_M}\left(\mathcal{D}_{MN}\frac{\partial v_1}{\partial X_N}\right) + f_1(\mathbf{v}, t), \tag{9}$$

$$\frac{\partial v_i}{\partial t} = f_i(\mathbf{v}, t), \quad i = 2, 3, \ldots, N, \tag{10}$$

where $\mathbf{v}(\mathbf{X}, t) : \Re^N \times \Re \to \Re^N$ is the dependent variable of the system of equations with action potential $v_1(\mathbf{X}, t)$, $\mathcal{C}$ is the capacitance, χ is the membrane surface-to-volume ratio, $\mathcal{D}$ is the conductivity tensor, $\mathbf{f}(\mathbf{v}, t) : \Re^N \times \Re \to \Re^N$ is a prescribed function describing the changes in ion concentrations and membrane ionic currents, and N is the number of equations in the system. $\mathbf{f}$ is a highly nonlinear function, and N is typically around 20 for a reasonably complex electrophysiological model. This model neglects mechanical deformation of the tissue. To take account of the mechanical deformation we modify (9) as described by Nash and Panfilov (2004) to give, for $\mathbf{X} \in \Omega$ and $t_0 < t < t_1$:

$$\mathcal{C}\frac{\partial v_1}{\partial t} = \frac{1}{\chi \det(F)}\frac{\partial}{\partial X_M}\left(\det(F)\mathcal{D}_{MN}C^{-1}_{NL}\frac{\partial v_1}{\partial X_L}\right) + f_1(\mathbf{v}, t). \tag{11}$$

In contrast to Nash and Panfilov (2004) we enforce incompressibility of cardiac tissue, and use (3) to simplify (11):

$$\mathcal{C}\frac{\partial v_1}{\partial t} = \frac{1}{\chi}\frac{\partial}{\partial X_M}\left(\mathcal{D}_{MN}C^{-1}_{NL}\frac{\partial v_1}{\partial X_L}\right) + f_1(\mathbf{v}, t). \tag{12}$$

To close this system we require a boundary condition for v_1, and initial conditions for all components of $\mathbf{v}$. These are given by

$$\frac{\partial v_1}{\partial n} = 0, \quad \mathbf{X} \in \partial\Omega_0, \quad t_0 < t < t_1,$$
$$\mathbf{v}(\mathbf{X}, t_0) = \mathbf{v_0}(\mathbf{X}), \quad \mathbf{X} \in \Omega,$$

where $\partial/\partial n$ denotes the normal derivative and $\partial\Omega_0$ denotes the boundary of the undeformed body.

There are a large number of different functions **f** that have been proposed: for a collection of such functions see the cellML website (cellML) or Nickerson (2004).

2.3. The generation of active tensions

The active tension is a function of, amongst other things, the extension ratio in the direction of the fibre, denoted by λ_1, that may be calculated from a soft tissue model of the heart. By using (1) and (4) we may deduce that

$$\lambda_1 = \sqrt{2E^*_{11} + 1}.$$

The model of active tension generation described by Niederer et al. (2006)—which has been developed from the Hunter–McCulloch-ter Keurs model (Hunter et al., 1998)—may then be written for some state vector **w**:

$$\frac{\mathrm{d}\mathbf{w}}{\mathrm{d}t} = \mathbf{g}\left(\mathbf{w}, \lambda_1, \frac{\mathrm{d}\lambda_1}{\mathrm{d}t}, \left[\mathrm{Ca}^{2+}\right]_i\right), \tag{13}$$

$$T_a = h(\mathbf{w}), \tag{14}$$

where **g** and **h** are prescribed nonlinear functions. The precise form of these equations are given in Appendix B.

3. Numerical simulations in one dimension

We simulate a fibre of cardiac cells that occupies the region $0 < X < 10$ mm. We use the electrophysiological model described by Noble et al. (1998) to simulate the electrical activity of the heart. The governing equations for this model are summarised in Appendix A. (2) and (3) are used to simulate the mechanical activity. The electrical and mechanical activity are coupled using the model of Niederer et al. (2006). The governing equations for this model are listed in Appendix B. Note that both the electrophysiological cell model and the coupling model that we use contain a differential equation that models the binding kinetics of troponin C and calcium—(A.1) for the model described by Noble et al. (1998) and (B.1) for the model described by Niederer et al. (2006). We use the equation from Niederer et al. (2006) as this takes account of the effect of actively developed tension on the unbinding rate of calcium from troponin. In common with ten Tusscher et al. (2004) we take $\mathcal{D}/(\chi\mathcal{C}) = 0.154$ mm/ms in (10). We take $\rho = 1.05 \times 10^{-6}$ kPa mm^{-2} s^2 as used by Schneider et al. (2000). Stimulation is performed at the end $X = 0$ which is fixed. The other end of the fibre is stress-free: this is modelled by the boundary condition $\partial x/\partial X = 1$ at $X = 10$ mm.

Before we can perform this simulation we need (i) a suitable stress–strain relationship and (ii) a suitable numerical method for computing the solution. We have described how the strain energy function given by (7) may be used with (8) to calculate a strain tensor in three dimensions. In Section 3.1 we explain how this strain energy function may be used to calculate a stress–strain relationship for use with a fibre that takes account of three dimensional properties. The numerical methods currently used lead to instabilities in the numerical solution, and so in Section 3.2 we develop the numerical methods that are currently used to ensure numerical stability of the resulting scheme.

3.1. The stress–strain relationship

Using the strain energy function (7) we derive a stress–strain relationship for one dimensional simulations by considering uniaxial extension and compression of cardiac fibres in the absence of active tensions. Other authors (Hunter et al. 1997, 1998) have used uniaxial tension to derive a stress–strain relationship in this way, but made the assumption that any deformation perpendicular to the axis of the fibre is independent of direction, and so $a_2 = a_3$, $b_2 = b_3$ and $k_2 = k_3$ in (7). In addition in this previous work, in the entries of T_{MN} given by (8), the term that was used to enforce incompressibility corresponds to the Cauchy stress tensor and not the 2nd Piola–Kirchoff stress tensor. These two stress tensors model different quantities: the entries of the Cauchy stress tensor are the force per unit *deformed* area acting on the *deformed* body; the entries of the 2nd Piola–Kirchoff stress tensor are the force per unit *undeformed* area acting on the *undeformed* body. Using terms from the Cauchy stress tensor when the theory is based on the 2nd Piola–Kirchoff stress tensor does not correctly enforce incompressibility.

For the analysis that follows we assume that the axes coincide with those aligned with the fibre and fibre sheet, and so there is no need to distinguish the axes in which the tensor is defined. As such we neglect the superscript * for these tensors and proceed by seeking a solution

$$x_1 = x_1(X_1), \qquad x_2 = x_2(X_2), \qquad x_3 = x_3(X_3),$$

giving

$$F = \begin{pmatrix} x_1'(X_1) & 0 & 0 \\ 0 & x_2'(X_2) & 0 \\ 0 & 0 & x_3'(X_3) \end{pmatrix},$$

$$E = \frac{1}{2}\begin{pmatrix} (x_1'(X_1))^2 - 1 & 0 & 0 \\ 0 & (x_2'(X_2))^2 - 1 & 0 \\ 0 & 0 & (x_3'(X_3))^2 - 1 \end{pmatrix}, \tag{15}$$

$$C^{-1} = \begin{pmatrix} (2E_{11}+1)^{-1} & 0 & 0 \\ 0 & (2E_{22}+1)^{-1} & 0 \\ 0 & 0 & (2E_{33}+1)^{-1} \end{pmatrix}.$$

Using (8) we may write

$$T = \begin{pmatrix} \frac{\partial W}{\partial E_{11}} - \frac{p}{2E_{11}+1} & 0 & 0 \\ 0 & \frac{\partial W}{\partial E_{22}} - \frac{p}{2E_{22}+1} & 0 \\ 0 & 0 & \frac{\partial W}{\partial E_{33}} - \frac{p}{2E_{33}+1} \end{pmatrix}. \tag{16}$$

The undeformed body is subject only to a force acting in the direction of the fibre and so we may write

$$T_{22} = T_{33} = 0. \tag{17}$$

A further relation is the incompressibility constraint

$$(2E_{11}+1)(2E_{22}+1)(2E_{33}+1) = 1. \tag{18}$$

We now derive a relationship between stress and strain separately for extension (where $E_{11} > 0$) and compression (where $E_{11} < 0$).

3.1.1. Extension of the fibre

For extension $E_{11} > 0$ and $E_{22}, E_{33} < 0$, and so $\partial W/\partial E_{22} = \partial W/\partial E_{33} = 0$. (16) gives

$$T_{22} = -\frac{p}{2E_{22}+1}, \qquad T_{33} = -\frac{p}{2E_{33}+1},$$

and (17) then implies $p = 0$. We may now use (16) to write

$$T_{11} = \frac{\partial W}{\partial E_{11}} = \frac{k_1 E_{11}}{(a_1 - E_{11})^{b_1}}\left(2 + \frac{b_1 E_{11}}{a_1 - E_{11}}\right), \quad E_{11} > 0. \tag{19}$$

3.1.2. Compression of the fibre

For compression $E_{11} < 0$ and $E_{22}, E_{33} > 0$. (16) and (17) give

$$\frac{\partial W}{\partial E_{22}} - \frac{p}{2E_{22}+1} = 0, \tag{20}$$

$$\frac{\partial W}{\partial E_{33}} - \frac{p}{2E_{33}+1} = 0. \tag{21}$$

Given a value of E_{11}, we may solve (18), (20) and (21) to give values of p, E_{22} and E_{33}. Finally, noting that $\partial W/\partial E_{11} = 0$ for $E_{11} < 0$, (16) implies that

$$T_{11} = -\frac{p}{2E_{11}+1}, \quad E_{11} < 0. \tag{22}$$

Using the parameters given by Remme et al. (2005) we plot the relationship between E_{11} and T_{11} given by (19) and (22) in Fig. 1.

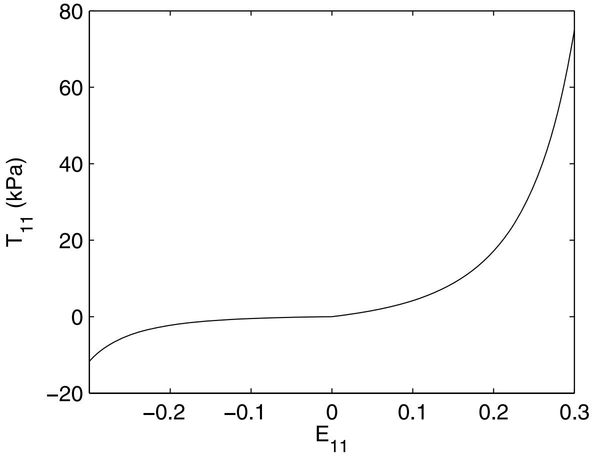

Fig. 1 The relationship between E_{11} and T_{11} given by (19) and (22).

3.2. *Numerical methods*

Unless otherwise stated, we discretise in space using 100 equally spaced points in our simulations. The effect of using more points was tested, but gave no noticeable difference to the solution. Spatial derivatives occur in the equations governing the transmembrane potential, (10), and the tissue deformation, (2). We use the finite element method in space for both of these quantities. In common with other authors (Smith et al., 2004; Nickerson et al., 2005) we use a continuous piecewise linear approximation was used for the transmembrane potential and a cubic Hermite approximation was used for the tissue deformation. We compute the mechanical deformations by writing (2) as the first order system of equations

$$\frac{\partial x_1}{\partial t} = u_1, \tag{23}$$

$$\rho \frac{\partial u_1}{\partial t} = \frac{\partial}{\partial X_1}\left(T_{11}\frac{\partial x_1}{\partial X_1}\right), \tag{24}$$

where u_1 is the velocity. As discussed earlier, other authors assume that deformations occur instantaneously. This assumption is equivalent to writing $\rho = 0$ in (2). We may test the validity of this assumption by setting $\rho = 0$ in (24) and neglecting (23).

3.2.1. *Previously used methods for discretising in time*

Other workers who have coupled the electrical and mechanical activity of the heart (Smith et al., 2004; Nickerson et al., 2005) have suggested updating (2) using a timestep of 1 ms, and other equations using a timestep of 0.01 ms. Such an approach requires using values of λ_1 and $\mathrm{d}\lambda_1/\mathrm{d}t$ calculated at a previous timestep when updating the electromechanical cell model using (13) and (14). This approach therefore necessitates at least a partially explicit approximation to time derivatives in any equations that contain the quantities λ_1 or $\lambda_1/\mathrm{d}t$—namely the equations arising from the model described by Niederer et al. (2006)

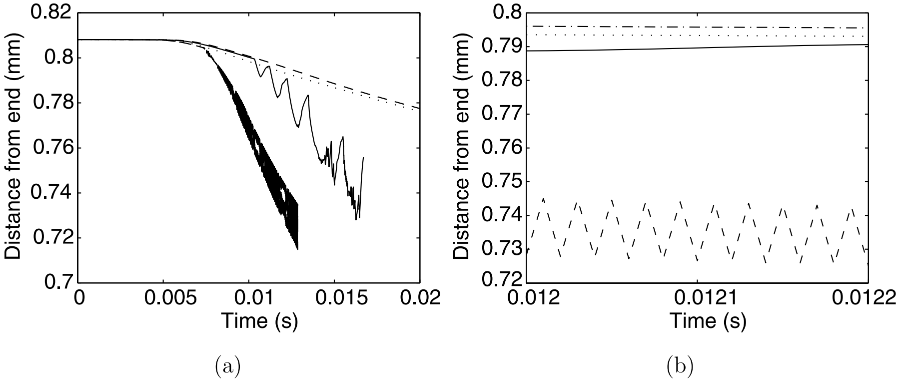

Fig. 2 The displacement of one node of the finite element scheme when the mechanical activity is updated separately from the electrical activity. The solid line refers to $\rho = 1.05 \times 10^{-6}$ kPa mm^{-2} s^2, the broken line to $\rho = 0$. The true solution is shown by the dot-dashed line for $\rho = 1.05 \times 10^{-6}$ kPa mm^{-2} s^2, and the dotted line for $\rho = 0$. (a) shows the solution until the displacements become too big for the pole–zero strain energy function to hold, (b) shows a magnified portion of (a).

that are given in Appendix B. This approach cannot be guaranteed to be numerically stable.

To investigate the stability of this approach, we update separately both the mechanics and the electrics using a timestep of 0.01 ms. Fully implicit backward Euler approximations are used for all time derivatives in the problem with the exception of the terms in the equations that include the quantities λ_1 or $d\lambda_1/dt$, as described in the previous paragraph: for these equations as many of the terms as possible were treated implicitly in order to give the scheme the maximum chance of being numerically stable. In Fig. 2, we plot the position of the 9th node as a function of time. The solid line corresponds to the simulation with $\rho = 1.05 \times 10^{-6}$ kPa mm^{-2} s^2, the broken line to $\rho = 0$. We have also plotted the true solution in this figure, which we describe how to calculate later. The dot-dashed line corresponds to the true solution with $\rho = 1.05 \times 10^{-6}$ kPa mm^{-2} s^2, the dotted line to the true solution with $\rho = 0$. We see from Fig. 2a that both values of ρ eventually lead to instabilities in the displacement, and eventually the simulation is terminated because the strains computed were outside the range of the strain energy function given by (7). In Fig. 2b a small region of Fig. 2a is magnified. Even when the timestep was reduced to 1.0×10^{-8} s, the same instability is observed. In the next section, we explain why this numerical approach is not appropriate. We then present a numerical approach that is suitable.

3.2.2. The hyperbolic nature of the PDE governing mechanical deformations

In this section, we show that the equation that arises from neglecting the left-hand side of (24) by writing $\rho = 0$ is at least partially hyperbolic when the stress tensor includes an active tension component as in (8). This explains why the explicit method used in the previous section was always unstable even when we reduced our timestep to many orders of magnitude smaller to the shortest timescale in the problem.

From (B.2) we may re-write the equation for Q_i as a "fading memory" integral equation:

$$Q_i = A_i \int_{-\infty}^{t} \mathrm{e}^{-\alpha_i(t-\tau)} \frac{\mathrm{d}\lambda}{\mathrm{d}\tau} \,\mathrm{d}\tau, \quad i = 1, 2, 3.$$

Q_i is therefore a weighted average of $\frac{\mathrm{d}\lambda}{\mathrm{d}\tau}$, heavily weighted towards the value when $t = \tau$. Using any numerical approximation to this integral, together with (B.3) allows us to write

$$Q(t) = K_{\lambda_1}\dot{\lambda}(t) + K_{\lambda_2}, \tag{25}$$

where K_{λ_2} is a function of values of $\dot{\lambda}$ at times less than t, which are assumed known. Using (B.4), we may then write

$$T_a = T_0 f_Q(Q),$$

for a suitable function f_Q. Alternatively, on noting that $\dot{\lambda} = \partial^2 x/(\partial X \partial t)$, and using (25),

$$T_a = T_0 f_\lambda\left(\frac{\partial^2 x}{\partial X \partial t}\right),$$

for a suitable function f_λ. (8) then allows us to write

$$T_{11} = \frac{\partial W}{\partial E_{11}} - p\left(\frac{\partial x}{\partial X}\right)^{-2} + T_0 f_\lambda\left(\frac{\partial^2 x}{\partial X \partial t}\right)\left(\frac{\partial x}{\partial X}\right)^{-2}.$$

Using (24) we may deduce that, for $T_0 \neq 0$, we have a third order derivative,

$$\frac{\partial^3 x}{\partial t\, \partial^2 X},$$

in our governing equation. The slopes of the characteristics of a third order partial differential equation are given by the solution of a cubic polynomial, and so will therefore have at least one real root. It is the presence of this real root that gives at least some hyperbolic nature to the governing equation. Hyperbolic partial differential equations are notoriously hard to solve numerically as some simple schemes are unconditionally unstable—see Morton and Mayers (1994) for a detailed discussion. In the next section, we describe a technique that does not suffer from numerical instability.

3.2.3. Proposed methods for discretising in time

In order to ensure stability of the governing equations, we repeat the simulations described above using a backward Euler approximation to all time derivatives, which requires us to update both the mechanical and electrical activity using the same timestep. The results of these simulations are shown in Fig. 3, where the solid line corresponds to the simulation with $\rho = 1.05 \times 10^{-6}$ kPa mm^{-2} s^2, and the broken line to $\rho = 0$. In Fig. 3a both lines are indistinguishable. The fibre contracts at the rate that would be expected. Relaxation to the undeformed state is slower than would be expected—we discuss this later.

In Fig. 3b—where the initial period of contraction shown in Fig. 3a is magnified—we see that there is a only very small period of time where the solution with $\rho = 0$ differs from

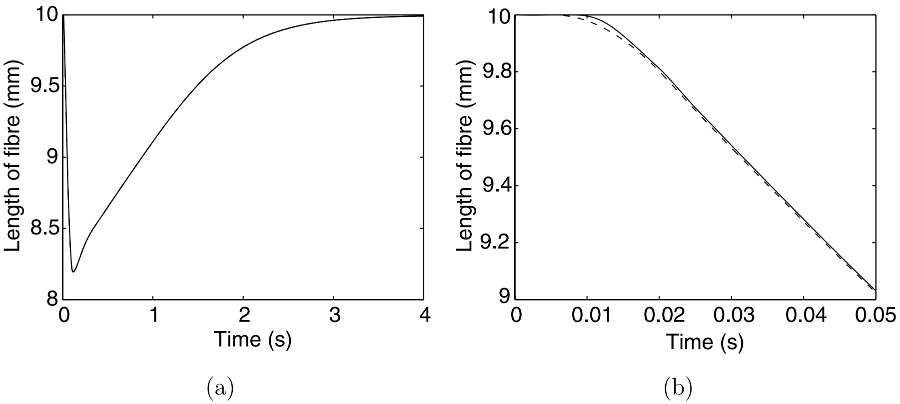

Fig. 3 The length of the fibre when both the mechanics and the electrics are updated using a stable numerical scheme. The solid line refers to $\rho = 1.05 \times 10^{-6}$ kPa mm^{-2} s^2, the broken line to $\rho = 0$. (a) shows the solution over the time interval $0 < t < 4$ s, (b) shows a magnified portion of (a).

the solution with $\rho = 1.05 \times 10^{-6}$ kPa mm^{-2} s^2. The difference between the solutions is insignificant, and so the approximation $\rho = 0$ is a valid approximation. The insignificance of the acceleration term on the left hand side of (2) may be deduced by considering the magnitude of the quantities appearing in this equation. From Fig. 3a we see that changes in x are of order 1.8 mm and changes in T are of order 0.9 kPa. Noting that this happens over the interval $0 < X < 10$ mm and a time interval of around 0.115 s, we see that, for $\rho = 1.05 \times 10^{-6}$ kPa mm^{-2} s^2, the acceleration term is over two orders of magnitude smaller than the right hand side of this equation and so may be neglected with minimal error. We would, however, suggest using $\rho = 1.05 \times 10^{-6}$ kPa mm^{-2} s^2 when solving these equations, as this leads to faster convergence of the nonlinear solver.

We conclude this section by showing plots of the transmembrane potential, calcium transient, length of fibre and active tension generated during the time interval $0 < t < 0.5$ s. These may all be seen in Fig. 4.

4. Results of the simulations

4.1. *The timescale for the extension ratio* λ_1

In Section 3.2.3 we demonstrated that the approximation $\rho = 0$ is valid. A consequence of this assumption is that the deformation of heart tissue may be modelled as an instantaneous reaction to the generation of active tensions. We therefore expect the quantity λ_1—and therefore $\mathrm{d}\lambda_1/\mathrm{d}t$—to vary very rapidly with time. This is confirmed in Fig. 5 where we plot the value of $\mathrm{d}\lambda_1/\mathrm{d}t$ at the midpoint of the fibre. The rapid variation of $\mathrm{d}\lambda_1/\mathrm{d}t$ is particularly apparent in Fig. 5b where a small portion of Fig. 5a has been magnified. We see from (B.2–B.4) that the active tension used when calculating the mechanical deformations is dependent upon the quantity $\mathrm{d}\lambda_1/\mathrm{d}t$. As $\mathrm{d}\lambda_1/\mathrm{d}t$ is calculated from the mechanical activity, an accurate calculation of $\mathrm{d}\lambda_1/\mathrm{d}t$ requires that this component of the

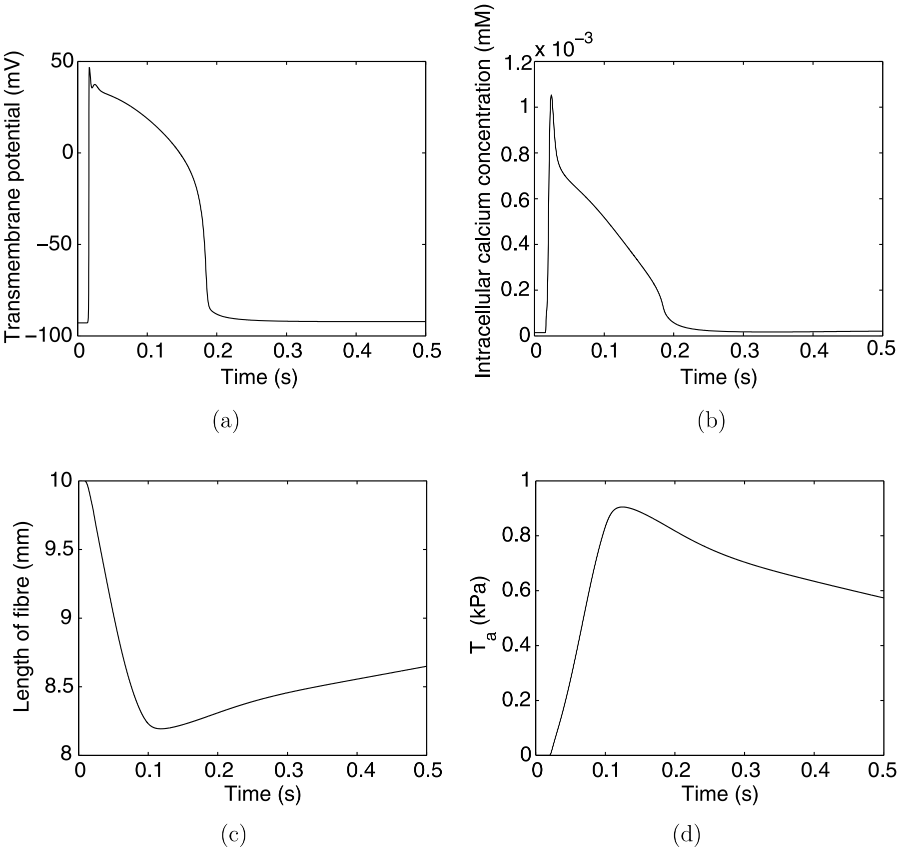

(a)

(b)

(c)

(d)

Fig. 4 The results of the simulation where a stable numerical scheme was used. (a) The transmembrane potential. (b) The calcium transient. (c) The length of the fibre. (d) The active tension generated.

whole problem should be updated much more frequently than every 1 ms as is proposed by other workers.

We now turn our attention to investigating the choice of timestep and mesh spacing that should be used when calculating the numerical solution of the coupled system. Accurate computation of the transmembrane potential may be achieved with a timestep of 0.1 ms providing the numerical scheme chosen is numerically stable (Whiteley, 2006). In Fig. 6a we investigate choice of timestep on the length of the deformed fibre. We use the same spatial mesh as before, but in these simulations we use a timestep of 0.1 ms (solid line), 0.2 ms (broken line) and 0.5 ms (dotted line). Note that we use the same timestep for both the electrical and mechanical component of the model. While a timestep of 0.5 ms would give a large error in the computation of the action potential (Whiteley, 2006), this error does not pollute the computation of the contraction of the fibre. A timestep of 0.5 ms does not accurately compute $\mathrm{d}\lambda_1/\mathrm{d}t$ as shown in Fig. 5b—we may therefore conclude that the mechanical deformation of the fibre is only weakly dependent on $\mathrm{d}\lambda_1/\mathrm{d}t$ in this case.

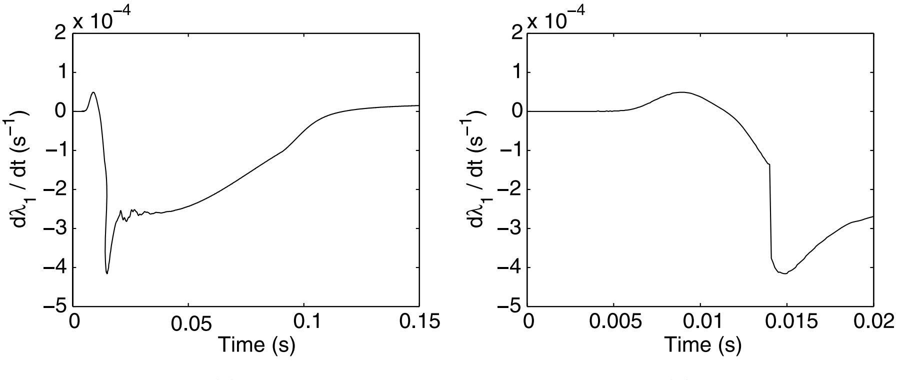

(a) (b)

Fig. 5 $d\lambda_1/dt$ calculated at $X = 0.5$ mm. (b) shows a magnified portion of (a).

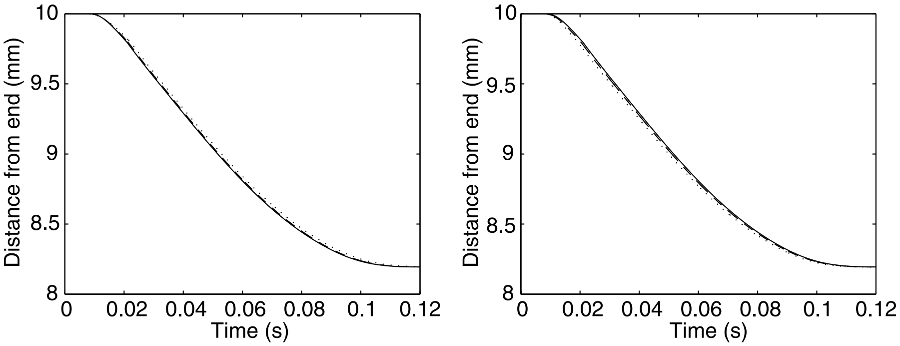

(a) (b)

Fig. 6 (a) The length of the fibre calculated using different timesteps: 0.1 ms (solid line); 0.2 ms (broken line); and 0.5 ms (dotted line). (b) The length of the fibre calculated using different space steps: 0.1 mm (solid line); 0.2 mm (broken line); and 0.4 mm (dotted line).

In Fig. 6b, we use a timestep of 0.1 ms and investigate the spacing between nodes: 0.1 mm (solid line); 0.2 mm (broken line); and 0.4 mm (dotted line). We see that the contraction of the fibre is not unduly affected by increasing the spacing between nodes from 0.1 mm to 0.4 mm.

4.2. A demonstration of the mechanical activity of the heart affecting the electrical activity of the heart

There is a large body of work where electrophysiological cell models are used to model the electrical activity of the whole heart, neglecting the influence of the deformation of the heart. This is equivalent to solving (12) with the matrix C equal to the identity matrix. In Fig. 7, we stimulate the end of the fibre $X = 0$ every 0.18 s. In Fig. 7a, we take account of deformations of the heart when solving (12). In Fig. 7b, we neglect the ef-

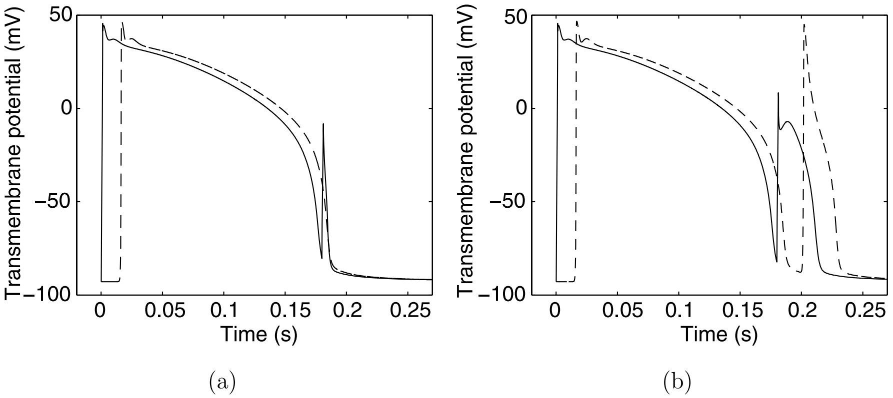

Fig. 7 The transmembrane potential at $X = 0$ (solid line) and $X = 10$ mm (broken line). (a) shows the simulation when using (12), (b) shows the simulation when the mechanical deformation is neglected in (12).

fect of deformations of the heart when solving (12). In both figures, the solid line is the transmembrane potential at the stimulated end ($X = 0$), and the broken line is the transmembrane potential at the other end of the fibre ($X = 10$ mm). We see that in Fig. 7a the stimulus at $t = 0.18$ s is not sufficient to generate an action potential that propagates along the deformed fibre. However, in Fig. 7b an action potential is propagated along the fibre, where no account has been taken of deformation of the fibre. This is an example of a situation where the electrical activity of the heart depends significantly on the mechanical activity. When taking account of heart deformations, the action potential propagates along the deformed fibre: If an action potential is generated when the fibre has contracted, the far end of the fibre is nearer and so it can reach it faster. As a result, the stimulation may arrive during the refractory period and so an action potential will not be generated.

We should point out that in the simulation described above there is only a very small window where a stimulus will generate a propagating action potential when the mechanical deformation is neglected, and no propagating action potential when the mechanical deformation is taken into account. In general, the electrical activity of the heart is only very weakly dependent on the mechanical activity. Nevertheless, given the dramatic effect, when simulating the electrical activity of the heart the possibility of this phenomenon should always be considered.

4.3. The effect of $[\mathrm{Ca}^{2+}]_i$ *on* T_a

The model described by Niederer et al. (2006) requires $[\mathrm{Ca}^{2+}]_i$ as input from an electrophysiological cell model. As such, it seems sensible to investigate the effect of $[\mathrm{Ca}^{2+}]_i$ on T_a predicted by the numerical techniques we have used in this study. It has been observed experimentally (Choi and Salama, 2000) that the amplitude of the $[\mathrm{Ca}^{2+}]_i$ transient may be lowered significantly by pacing the heart at a faster frequency. In order to model this, we pace our fibre at different frequencies. We simulate until a regular pattern emerges and then record the amplitudes of $[\mathrm{Ca}^{2+}]_i$ and T_a. In Fig. 8a, we plot the amplitude of the $[\mathrm{Ca}^{2+}]_i$ transient against the interval between successive stimulations and observe that the

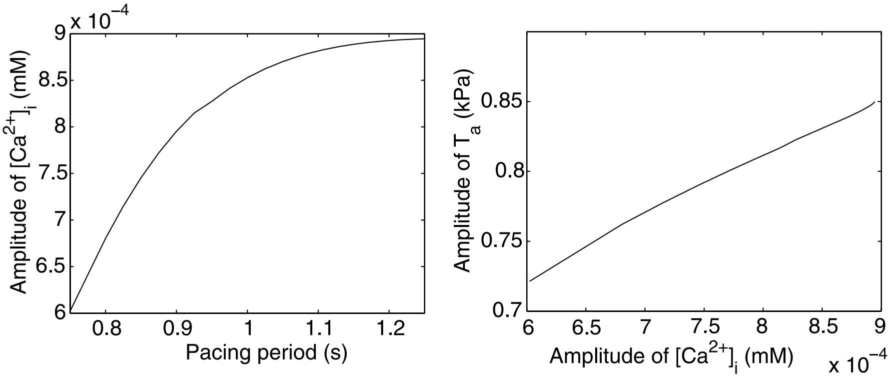

(a) (b)

Fig. 8 (a) The amplitude of the $[\mathrm{Ca}^{2+}]_i$ transient as a function of the pacing period. (b) The amplitude of the active tension as a function of the $[\mathrm{Ca}^{2+}]_i$ transient.

amplitude of the $[\mathrm{Ca}^{2+}]_i$ transient decreases when the fibre is stimulated more frequently, in agreement with Choi and Salama (2000). In Fig. 8b, we see that the amplitude of the active tension generated increases with the amplitude of the $[\mathrm{Ca}^{2+}]_i$ transient. As a consequence, the model used predicts that the amplitude of the active tension will be lower when the fibre is stimulated more frequently.

5. Discussion

We have coupled: (i) the electrophysiological model described by Noble et al. (1998); (ii) a soft tissue model of a cardiac fibre that takes account of some three-dimensional properties; and (iii) a model that may be used to describe the generation of active tensions (Niederer et al., 2006). We identified why the simplest numerical techniques did not work for this coupled problem, and the identified suitable numerical methods for the coupling of these models. This allowed us to perform numerical simulations and carry out convergence tests without requiring excessive computing time.

Our first simulations were concerned with verifying the universally made assumption that cardiac tissue may be modelled as having zero density. While this assumption is valid for the simulations carried out in this study, we do not recommend using it, as the nonlinear solver used when solving the system of differential equations converged faster when the true (nonzero) value of density was used. We used the results of these simulations to argue that the validity of the assumption of zero density implied that λ_1 and $\mathrm{d}\lambda_1/\mathrm{d}t$ varied rapidly with time—while the simulations carried out in this study were not heavily dependent on these rapid variations, it is possible that simulations in higher dimensions may be affected.

We observed that the deformation of the cardiac fibre shown in Fig. 3a did not return to its original value as quickly as expected. This is partly because we have not modelled the force that would be exerted on the fibre by the heart filling with blood as would be seen in a realistic whole-heart model. However, the fact that the fibre has not returned to its undeformed state within 1 second indicates that a significant active tension is still acting at this time. This may be because the parameters used in the model of active tension are only very rarely measured at temperatures greater than 22°C (see Niederer et al., 2006). Simnett et al. (1998) have demonstrated that the relaxation transient occurs on a much faster timescale at 20°C compared to 12°C—it is therefore possible that the coupled model may predict a much faster relaxation if parameters measured at 37°C were available. Another possible explanation is that there is always considerable active tension in heart muscle fibres. More experimental research is required to identify the correct explanation of these observations.

Although the mechanical activity of the heart is more dependent on the electrical activity than electrical activity on mechanical activity, we did manage to demonstrate in Fig. 7a situation where the electrical activity of the heart depends significantly on the mechanical activity. In this case, during rapid pacing, we demonstrated that if the mechanical activity of the heart were neglected then an action potential did propagate along the fibre. If mechanical activity was taken account of, the action potential did not propagate. Realistic whole-heart electrical simulations should therefore consider the possibility that heart deformations may affect the propagation of an action potential.

Appendix A The electrophysiological cell model used

Below we summarise the equations given by Noble et al. (1998) that are used in (9) and (10).

A.1 Initial values

Quantity	Symbol	Initial value	Unit
First of two gates for the ACh dependent potassium current	$ActFrac$	0.0042614	none
Second of two gates for the ACh dependent potassium current	$ProdFrac$	0.4068154	none
Inactivation gate of fast sodium current	h	0.9944036	none
Activation gate of fast sodium current	m	0.0016203	none
Calcium bound to calmodulin	Ca_{Calmod}	0.0005555	mM
Calcium concentration in the diadic subspace	Ca_{ds}	1.88×10^{-5}	mM
Intracellular calcium concentration	Ca_i	1.4×10^{-5}	mM
Calcium concentration in the junctional SR release store	Ca_{rel}	0.4481927	mM
Calcium bound to troponin	Ca_{Trop}	0.0003542	mM
Calcium concentration in the network SR uptake store	Ca_{up}	0.4531889	mM
Intracellular potassium concentration	K_i	136.5644281	mM
Intracellular sodium concentration	Na_i	7.3321223	mM
Activation gate of the L-type calcium channel	d	0	none
First inactivation gate for L-type calcium current	f	1	none
Second inactivation gate for L-type calcium current in the membrane outside the diadic subspace	f_2	0.9349197	none
Second inactivation gate for L-type calcium current in the membrane when open into the diadic subspace	f_{2ds}	0.9651958	none
Transmembrane potential	V	−92.849333	mV
Fast gate of rapid component of delayed rectifier current	x_{r1}	1.03×10^{-5}	none
Slow gate of rapid component of delayed rectifier current	x_{r2}	2×10^{-7}	none

Slow component of delayed rectifier current	x_s	0.001302	none
Second gate of transient outward current	r	0	none
First gate of transient outward current	s	0.9948645	none

A.2 Parameter values

	Value	Unit
g_{bca}	0.00025	µS
$K_{leak_{rate}}$	0.05	s^{-1}
$Km_{Ca_{cyt}}$	0.0005	mM
$Km_{Ca_{ds}}$	0.01	mM
Km_{rel}	250	s^{-1}
Ca_o	2	mM
K_o	4	mM
Na_o	140	mM
g_{Na}	2.5	µS
δ_m	1×10^{-5}	none
α_{Calmod}	100,000	s^{-1}
α_{Trop}	100,000	s^{-1}
β_{Calmod}	50	s^{-1}
β_{Trop}	200	s^{-1}
$Calmod$	0.02	mM
$Kdecay$	10	s
$length$	74	µm
$radius$	12	µm
$Trop$	0.05	mM
$V_{ds_{ratio}}$	0.1	none
$V_{e_{ratio}}$	0.4	none
$V_{rel_{ratio}}$	0.1	none
$V_{up_{ratio}}$	0.01	none
$speed_d$	3	none
δ_f	0.0001	none
$speed_f$	0.3	none
$FrICa$	1	none
Km_{f2}	100,000	mM
Km_{f2ds}	0.001	mM
P_{Ca_L}	0.1	nA/mM
P_{CaK}	0.002	nA/mM
P_{CaNa}	0.01	nA/mM
R_{decay}	20	mM/s
Cm	9.5×10^{-5}	µF
F	96,485.3415	C/M
R	8,314.472	mJ/(M K)
T	310	K
g_{pna}	0.004	µS
g_{Kr1}	0.0021	µS
g_{Kr2}	0.0013	µS
P_{kna}	0.03	nA/mM
α_{up}	0.4	s^{-1}
β_{up}	0.03	s^{-1}
K_{cyca}	0.0003	mM
K_{srca}	0.5	mM
K_{xcs}	0.4	mM

g_{Ks}	0.0026	µS
g_{bna}	0.0006	µS
d_{NaCa}	0	none
$FRiNaCa$	0.001	none
$gamma$	0.5	none
k_{NaCa}	0.0005	nA
n_{NaCa}	3	none
$i_{NaK_{max}}$	0.7	nA
K_{mK}	1	mM
K_{mNa}	40	mM
g_{K1}	0.5	µS
K_{mk1}	10	mM
g_{to}	0.005	µS
g_{tos}	0	µS

A.3 The differential equations

A.3.1 Calcium background current

$$i_{b_{Ca}} = g_{bca} \cdot (V - E_{Ca}).$$

A.3.2 Calcium release

$$\begin{aligned}
&VoltDep = e^{0.08\cdot(V-40)},\\
&CaiReg = \frac{Ca_i}{Ca_i + K_{m_{Ca_{cyt}}}},\\
&CadsReg = \frac{Ca_{ds}}{Ca_{ds} + K_{m_{Ca_{ds}}}},\\
&RegBindSite = CaiReg + (1 - CaiReg) \cdot CadsReg,\\
&ActRate = 0 \cdot VoltDep + 500 \cdot RegBindSite^2,\\
&InactRate = 60 + 500 \cdot RegBindSite^2,\\
&SpeedRel = \begin{cases} 5 & \text{if } V < -50,\\ 1 & \text{otherwise,} \end{cases}\\
&PrecFrac = 1 - ActFrac - ProdFrac,\\
&\frac{\mathrm{d}ActFrac}{\mathrm{d}time} = PrecFrac \cdot SpeedRel \cdot ActRate - ActFrac \cdot SpeedRel \cdot InactRate,\\
&\frac{\mathrm{d}ProdFrac}{\mathrm{d}time} = ActFrac \cdot SpeedRel \cdot InactRate - SpeedRel \cdot ProdFrac,\\
&i_{rel} = \left(\left(\frac{ActFrac}{ActFrac + 0.25}\right)^2 \cdot K_{m_{rel}} + K_{leak_{rate}}\right) \cdot Ca_{rel}.
\end{aligned}$$

A.3.3 Calcium translocation

$$i_{trans} = 50 \cdot (Ca_{up} - Ca_{rel}).$$

A.3.4 Fast sodium current

$$i_{Na} = g_{Na} \cdot m^3 \cdot h \cdot (V - E_{mh}).$$

A.3.5 Fast sodium current h gate

$$\alpha_h = 20 \cdot e^{-0.125 \cdot (V+75)},$$

$$\beta_h = \frac{2{,}000}{1 + 320 \cdot e^{-0.1 \cdot (V+75)}},$$

$$\frac{\mathrm{d}h}{\mathrm{d}time} = \alpha_h \cdot (1-h) - \beta_h \cdot h.$$

A.3.6 Fast sodium current m gate

$$E0_m = V + 41,$$

$$\alpha_m = \begin{cases} 2{,}000 & \text{if } |E0_m| < \delta_m, \\ \dfrac{200 \cdot E0_m}{1 - e^{-0.1 \cdot E0_m}} & \text{otherwise,} \end{cases}$$

$$\beta_m = 8{,}000 \cdot e^{-0.056 \cdot (V+66)},$$

$$\frac{\mathrm{d}m}{\mathrm{d}time} = \alpha_m \cdot (1-m) - \beta_m \cdot m.$$

A.3.7 Intracellular calcium concentration

$$\begin{aligned}
V_{Cell} &= \frac{3.141592654 \cdot (\frac{radius}{1{,}000})^2 \cdot length}{1{,}000}, \\
V_{i_{ratio}} &= 1 - V_{e_{ratio}} - V_{up_{ratio}} - V_{rel_{ratio}}, \\
V_i &= V_{Cell} \cdot V_{i_{ratio}}, \\
\frac{\mathrm{d}Ca_i}{\mathrm{d}time} &= \frac{-1}{2 \cdot V_i \cdot F} \cdot (i_{Ca_{L_{Ca_{cyt}}}} + i_{b_{Ca}} - 2 \cdot i_{NaCa_{cyt}}) + Ca_{ds} \cdot V_{ds_{ratio}} \cdot Kdecay \\
&\quad + \frac{i_{rel} \cdot V_{rel_{ratio}}}{V_{i_{ratio}}} - \frac{\mathrm{d}Ca_{Calmod}}{\mathrm{d}time} - \frac{\mathrm{d}Ca_{Trop}}{\mathrm{d}time} - i_{up}, \\
\frac{\mathrm{d}Ca_{ds}}{\mathrm{d}time} &= \frac{-i_{Ca_{L_{Ca_{ds}}}}}{2 \cdot V_{ds_{ratio}} \cdot V_i \cdot F} - Ca_{ds} \cdot Kdecay, \qquad \text{(A.1)} \\
\frac{\mathrm{d}Ca_{up}}{\mathrm{d}time} &= \frac{V_{i_{ratio}}}{V_{up_{ratio}}} \cdot i_{up} - i_{trans}, \\
\frac{\mathrm{d}Ca_{rel}}{\mathrm{d}time} &= \frac{V_{up_{ratio}}}{V_{rel_{ratio}}} \cdot i_{trans} - i_{rel}, \\
\frac{\mathrm{d}Ca_{Calmod}}{\mathrm{d}time} &= \alpha_{Calmod} \cdot Ca_i \cdot (Calmod - Ca_{Calmod}) - \beta_{Calmod} \cdot Ca_{Calmod}, \\
\frac{\mathrm{d}Ca_{Trop}}{\mathrm{d}time} &= \alpha_{Trop} \cdot Ca_i \cdot (Trop - Ca_{Trop}) - \beta_{Trop} \cdot Ca_{Trop}.
\end{aligned}$$

A.3.8 Intracellular potassium concentration

$$\frac{\mathrm{d}K_i}{\mathrm{d}time} = \frac{-1}{V_i \cdot F} \cdot (i_{K1} + i_{Kr} + i_{Ks} + i_{Ca_{L_{K_{cyt}}}} + i_{Ca_{L_{K_{ds}}}} + i_{to} - 2 \cdot i_{NaK}).$$

A.3.9 Intracellular sodium concentration

$$\frac{\mathrm{d}Na_i}{\mathrm{d}time} = \frac{-1}{V_i \cdot F} \cdot (i_{Na} + i_{p_{Na}} + i_{b_{Na}} + 3 \cdot i_{NaK} + 3 \cdot i_{NaCa_{cyt}} + i_{Ca_{L_{Na_{cyt}}}} + i_{Ca_{L_{Na_{ds}}}}).$$

A.3.10 L type calcium channel

$$i_{Ca_{L_{Ca_{cyt}}}} = \frac{\frac{(1-FrICa)\cdot 4\cdot P_{Ca_L}\cdot d\cdot f\cdot f_2\cdot(V-50)\cdot F}{R\cdot T}}{1 - e^{\frac{-(V-50)\cdot F\cdot 2}{R\cdot T}}} \cdot \left(Ca_i \cdot e^{\frac{100\cdot F}{R\cdot T}} - Ca_o \cdot e^{\frac{-(V-50)\cdot F\cdot 2}{R\cdot T}}\right),$$

$$i_{Ca_{L_{K_{cyt}}}} = \frac{\frac{(1-FrICa)\cdot P_{CaK}\cdot P_{Ca_L}\cdot d\cdot f\cdot f_2\cdot(V-50)\cdot F}{R\cdot T}}{1 - e^{\frac{-(V-50)\cdot F}{R\cdot T}}} \cdot \left(K_i \cdot e^{\frac{50\cdot F}{R\cdot T}} - K_o \cdot e^{\frac{-(V-50)\cdot F}{R\cdot T}}\right),$$

$$i_{Ca_{L_{Na_{cyt}}}} = \frac{\frac{(1-FrICa)\cdot P_{CaNa}\cdot P_{Ca_L}\cdot d\cdot f\cdot f_2\cdot(V-50)\cdot F}{R\cdot T}}{1 - e^{\frac{-(V-50)\cdot F}{R\cdot T}}} \cdot \left(Na_i \cdot e^{\frac{50\cdot F}{R\cdot T}} - Na_o \cdot e^{\frac{-(V-50)\cdot F}{R\cdot T}}\right),$$

$$i_{Ca_{L_{Ca_{ds}}}} = \frac{\frac{FrICa\cdot 4\cdot P_{Ca_L}\cdot d\cdot f\cdot f_{2ds}\cdot(V-50)\cdot F}{R\cdot T}}{1 - e^{\frac{-(V-50)\cdot F\cdot 2}{R\cdot T}}} \cdot \left(Ca_i \cdot e^{\frac{100\cdot F}{R\cdot T}} - Ca_o \cdot e^{\frac{-(V-50)\cdot F\cdot 2}{R\cdot T}}\right),$$

$$i_{Ca_{L_{K_{ds}}}} = \frac{\frac{FrICa\cdot P_{CaK}\cdot P_{Ca_L}\cdot d\cdot f\cdot f_{2ds}\cdot(V-50)\cdot F}{R\cdot T}}{1 - e^{\frac{-(V-50)\cdot F}{R\cdot T}}} \cdot \left(K_i \cdot e^{\frac{50\cdot F}{R\cdot T}} - K_o \cdot e^{\frac{-(V-50)\cdot F}{R\cdot T}}\right),$$

$$i_{Ca_{L_{Na_{ds}}}} = \frac{\frac{FrICa\cdot P_{CaNa}\cdot P_{Ca_L}\cdot d\cdot f\cdot f_{2ds}\cdot(V-50)\cdot F}{R\cdot T}}{1 - e^{\frac{-(V-50)\cdot F}{R\cdot T}}} \cdot \left(Na_i \cdot e^{\frac{50\cdot F}{R\cdot T}} - Na_o \cdot e^{\frac{-(V-50)\cdot F}{R\cdot T}}\right),$$

$$i_{Ca_L} = i_{Ca_{L_{Ca_{cyt}}}} + i_{Ca_{L_{K_{cyt}}}} + i_{Ca_{L_{Na_{cyt}}}} + i_{Ca_{L_{Ca_{ds}}}} + i_{Ca_{L_{K_{ds}}}} + i_{Ca_{L_{Na_{ds}}}}.$$

A.3.11 L type calcium channel d gate

$$E0_d = V + 24 - 5,$$

$$\alpha_d = \begin{cases} 120 & \text{if } |E0_d| < 0.0001, \\ \frac{30\cdot E0_d}{1-e^{\frac{-E0_d}{4}}} & \text{otherwise,} \end{cases}$$

$$\beta_d = \begin{cases} 120 & \text{if } |E0_d| < 0.0001, \\ \frac{12\cdot E0_d}{e^{\frac{E0_d}{10}}-1} & \text{otherwise,} \end{cases}$$

$$\frac{\mathrm{d}d}{\mathrm{d}time} = speed_d \cdot \left(\alpha_d \cdot (1-d) - \beta_d \cdot d\right).$$

A.3.12 L type calcium channel f gate

$$E0_f = V + 34,$$

$$\alpha_f = \begin{cases} 25 & \text{if } |E0_f| < \delta_f, \\ \frac{6.25 \cdot E0_f}{e^{\frac{E0_f}{4}} - 1} & \text{otherwise,} \end{cases}$$

$$\beta_f = \frac{12}{1 + e^{\frac{-1 \cdot (V+34)}{4}}},$$

$$\frac{\mathrm{d}f}{\mathrm{d}time} = speed_f \cdot \big(\alpha_f \cdot (1 - f) - \beta_f \cdot f\big).$$

A.3.13 L type calcium channel f_2 gate

$$\frac{\mathrm{d}f_2}{\mathrm{d}time} = 1 - \left(\frac{Ca_i}{Km_{f2} + Ca_i} + f_2\right).$$

A.3.14 L type calcium channel f_{2ds} gate

$$\frac{\mathrm{d}f_{2ds}}{\mathrm{d}time} = R_{decay} \cdot \left(1 - \left(\frac{Ca_{ds}}{Km_{f2ds} + Ca_{ds}} + f_{2ds}\right)\right).$$

A.3.15 Membrane

$$\begin{aligned} I_{ion} = {} & i_{Stim} + i_{K1} + i_{to} + i_{Kr} + i_{Ks} + i_{NaK} + i_{Na} + i_{b_{Na}} + i_{p_{Na}} + i_{Ca_{L_{Na_{cyt}}}} \\ & + i_{Ca_{L_{Na_{ds}}}} + i_{NaCa_{cyt}} + i_{NaCa_{ds}} + i_{Ca_{L_{Ca_{cyt}}}} + i_{Ca_{L_{Ca_{ds}}}} + i_{Ca_{L_{K_{cyt}}}} \\ & + i_{Ca_{L_{K_{ds}}}} + i_{b_{Ca}}. \end{aligned}$$

A.3.16 Persistent sodium current

$$i_{p_{Na}} = \frac{g_{pna} \cdot 1}{1 + e^{\frac{-(V+52)}{8}}} \cdot (V - E_{Na}).$$

A.3.17 Rapid delayed rectifier potassium current

$$i_{Kr} = \frac{(g_{Kr1} \cdot x_{r1} + g_{Kr2} \cdot x_{r2}) \cdot 1}{1 + e^{\frac{V+9}{22.4}}} \cdot (V - E_K).$$

A.3.18 Rapid delayed rectifier potassium current x_{r1} gate

$$\alpha_{xr1} = \frac{50}{1 + e^{\frac{-(V-5)}{9}}},$$

$$\beta_{xr1} = 0.05 \cdot e^{\frac{-(V-20)}{15}},$$

$$\frac{\mathrm{d}x_{r1}}{\mathrm{d}time} = \alpha_{xr1} \cdot (1 - xr1t) - \beta_{xr1} \cdot x_{r1}.$$

A.3.19 Rapid delayed rectifier potassium current x_{r2} gate

$$\alpha_{xr2} = \frac{50}{1 + e^{\frac{-(V-5)}{9}}},$$

$$\beta_{xr2} = 0.4 \cdot e^{-(\frac{V+30}{30})^3},$$

$$\frac{\mathrm{d}x_{r2}}{\mathrm{d}time} = \alpha_{xr2} \cdot (1 - xr2) - \beta_{xr2} \cdot x_{r2}.$$

A.3.20 Reversal potentials

$$E_{Na} = \frac{R \cdot T}{F} \cdot \ln \frac{Na_o}{Na_i},$$

$$E_K = \frac{R \cdot T}{F} \cdot \ln \frac{K_o}{K_i},$$

$$E_{Ks} = \frac{R \cdot T}{F} \cdot \ln \frac{K_o + P_{kna} \cdot Na_o}{K_i + P_{kna} \cdot Na_i},$$

$$E_{Ca} = \frac{0.5 \cdot R \cdot T}{F} \cdot \ln \frac{Ca_o}{Ca_i},$$

$$E_{mh} = \frac{R \cdot T}{F} \cdot \ln \frac{Na_o + 0.12 \cdot K_o}{Na_i + 0.12 \cdot K_i}.$$

A.3.21 Sarcoplasmic reticulum calcium pump

$$K_1 = \frac{K_{cyca} \cdot K_{xcs}}{K_{srca}},$$

$$K_2 = Ca_i + Ca_{up} \cdot K_1 + K_{cyca} \cdot K_{xcs} + K_{cyca},$$

$$i_{up} = \frac{Ca_i}{K_2} \cdot \alpha_{up} - \frac{Ca_{up} \cdot K_1}{K_2} \cdot \beta_{up}.$$

A.3.22 Slow delayed rectifier potassium current

$$i_{Ks} = g_{Ks} \cdot x_s^2 \cdot (V - E_{Ks}).$$

A.3.23 Slow delayed rectifier potassium current x_s gate

$$\alpha_{xs} = \frac{14}{1 + e^{\frac{-(V-40)}{9}}},$$

$$\beta_{xs} = e^{\frac{-V}{45}},$$

$$\frac{\mathrm{d}x_s}{\mathrm{d}time} = \alpha_{xs} \cdot (1 - xs) - \beta_{xs} \cdot x_s.$$

A.3.24 Sodium background current

$$i_{b_{Na}} = g_{bna} \cdot (V - E_{Na}).$$

A.3.25 Sodium calcium exchanger

$$i_{NaCa_{cyt}} = (1 - FRiNaCa) \cdot k_{NaCa}$$

$$\times \frac{(e^{\frac{gamma \cdot (n_{NaCa} - 2) \cdot V \cdot F}{R \cdot T}} \cdot Na_i^{n_{NaCa}} \cdot Ca_o - e^{\frac{(gamma-1) \cdot (n_{NaCa} - 2) \cdot V \cdot F}{R \cdot T}} \cdot Na_o^{n_{NaCa}} \cdot Ca_i)}{(1 + d_{NaCa} \cdot (Ca_i \cdot Na_o^{n_{NaCa}} + Ca_o \cdot Na_i^{n_{NaCa}})) \cdot (1 + \frac{Ca_i}{0.0069})},$$

$$i_{NaCa_{ds}} = FRiNaCa \cdot k_{NaCa}$$

$$\times \frac{(e^{\frac{gamma \cdot (n_{NaCa} - 2) \cdot V \cdot F}{R \cdot T}} \cdot Na_i^{n_{NaCa}} \cdot Ca_o - e^{\frac{(gamma-1) \cdot (n_{NaCa} - 2) \cdot V \cdot F}{R \cdot T}} \cdot Na_o^{n_{NaCa}} \cdot Ca_{ds})}{(1 + d_{NaCa} \cdot (Ca_{ds} \cdot Na_o^{n_{NaCa}} + Ca_o \cdot Na_i^{n_{NaCa}})) \cdot (1 + \frac{Ca_{ds}}{0.0069})},$$

$$i_{NaCa} = i_{NaCa_{cyt}} + i_{NaCa_{ds}}.$$

A.3.26 Sodium potassium pump

$$i_{NaK} = \frac{\frac{i_{NaK_{max}} \cdot K_o}{K_{mK} + K_o} \cdot Na_i}{K_{mNa} + Na_i}.$$

A.3.27 Time_independent_potassium_current

$$i_{K1} = \frac{\frac{g_{K1} \cdot K_o}{K_o + K_{mk1}} \cdot (V - E_K)}{1 + e^{\frac{(V - E_K - 10) \cdot F \cdot 1.25}{R \cdot T}}}.$$

A.3.28 Transient outward current

$$i_{to} = g_{to} \cdot \big(g_{tos} + s \cdot (1 - g_{tos})\big) \cdot r \cdot (V - E_K).$$

A.3.29 Transient outward current r gate

$$\frac{\mathrm{d}r}{\mathrm{d}time} = 333 \cdot \left(\frac{1}{1 + e^{\frac{-(V+4)}{5}}} - r\right).$$

A.3.30 Transient outward current s gate

$$\alpha_s = 0.033 \cdot e^{\frac{-V}{17}},$$

$$\beta_s = \frac{33}{1 + e^{-0.125 \cdot (V+10)}},$$

$$\frac{\mathrm{d}s}{\mathrm{d}time} = \alpha_s \cdot (1 - s) - \beta_s \cdot s.$$

Appendix B The model used to generate active tensions

Below we summarise the equations given by Niederer et al. (2006).

B.1 *Initial values*

	Initial value	Units
$[\mathrm{Ca}^{2+}]_{\mathrm{Trpn}}$	0	μM
z	0	Dimensionless
$Q_i, \quad i = 1, 2, 3$	0	Dimensionless

B.2 *Parameter values*

	Value	Unit
k_{on}	100	$\mu\mathrm{M}^{-1}\,\mathrm{s}^{-1}$
k_{refoff}	200	s^{-1}
γ	2	Dimensionless
$[\mathrm{Ca}^{2+}]_{\mathrm{TrpnMax}}$	70	μM
α_{r_1}	2	s^{-1}
α_{r_2}	1.75	s^{-1}
K_Z	0.15	Dimensionless
n_r	3	Dimensionless
β_1	−4	Dimensionless
α_0	8	s^{-1}
n	3	Dimensionless
z_p	0.85	Dimensionless
$[\mathrm{Ca}^{2+}]_{50\mathrm{ref}}$	1.05	μM
T_{ref}	56.2	kPa
β_0	4.9	Dimensionless
a	0.35	Dimensionless
A_1	−29	Dimensionless
A_2	138	Dimensionless
A_3	129	Dimensionless
α_1	30	s^{-1}
α_2	130	s^{-1}
α_3	625	s^{-1}

B.3 *The differential equations*

$$\begin{aligned}\frac{\mathrm{d}}{\mathrm{d}t}[\mathrm{Ca}^{2+}]_{\mathrm{Trpn}} &= k_{\mathrm{on}}[\mathrm{Ca}^{2+}]_i\big([\mathrm{Ca}^{2+}]_{\mathrm{TrpnMax}} - [\mathrm{Ca}^{2+}]_{\mathrm{Trpn}}\big) \\ &\quad - k_{\mathrm{refoff}}\left(1 - \frac{T_a}{\gamma T_{\mathrm{ref}}}\right)[\mathrm{Ca}^{2+}]_{\mathrm{Trpn}},\end{aligned} \tag{B.1}$$

$$\frac{\mathrm{d}z}{\mathrm{d}t} = \alpha_0\left(\frac{[\mathrm{Ca}^{2+}]_{\mathrm{Trpn}}}{[\mathrm{Ca}^{2+}]_{\mathrm{Trpn50}}}\right)^n (1 - z) - \alpha_{r_1} z - \alpha_{r_2}\frac{z^{n_r}}{z^{n_r} + K_z^{n_r}},$$

$$[\mathrm{Ca}^{2+}]_{\mathrm{Trpn50}} = \frac{[\mathrm{Ca}^{2+}]_{\mathrm{TrpnMax}}[\mathrm{Ca}^{2+}]_{50\mathrm{ref}}(1 + \beta_1(\lambda_1 - 1))}{[\mathrm{Ca}^{2+}]_{50\mathrm{ref}}(1 + \beta_1(\lambda_1 - 1)) + \frac{k_{\mathrm{refoff}}}{k_{\mathrm{on}}}(1 - \frac{1+\beta_0(\lambda_1-1)}{2\gamma})},$$

$$K_1 = \frac{\alpha_{r_2} z_p^{n_r - 1} n_r K_z^{n_r}}{(z_p^{n_r} + K_z^{n_r})^2},$$

$$K_2 = \frac{\alpha_{r_2} z_p^{n_r}}{z_p^{n_r} + K_z^{n_r}} \left(1 - \frac{n_r K_Z^{n_r}}{z_p^{n_r} + K_z^{n_r}}\right),$$

$$z_{\max} = \frac{\alpha_0 - K_2[\mathrm{Ca}^{2+}]_{\mathrm{Trpn50}}}{\alpha_0 + (\alpha_{r_1} + K_1)[\mathrm{Ca}^{2+}]_{\mathrm{Trpn50}}},$$

$$T_0 = \frac{z T_{\mathrm{ref}}(1 + \beta_0(\lambda_1 - 1))}{z_{\max}},$$

$$\frac{\mathrm{d}Q_i}{\mathrm{d}t} = A_i \frac{\mathrm{d}\lambda_1}{\mathrm{d}t} - \alpha_i Q_i, \quad i = 1, 2, 3, \tag{B.2}$$

$$Q = Q_1 + Q_2 + Q_3, \tag{B.3}$$

$$T_a = \begin{cases} T_0 \frac{1+(2+a)Q}{1+Q} & Q > 0, \\ T_0 \frac{1+aQ}{1-Q} & Q \le 0. \end{cases} \tag{B.4}$$

References

cellML. http://www.cellml.org/examples/repository/index.html#cardiac_ep_models.

Choi, B.-R., Salama, G., 2000. Simultaneous maps of optical action potentials and calcium transients in guinea–pig hearts: mechanisms underlying concordant alternans. J. Physiol. 529, 171–188.

Costa, K.D., Holmes, J.W., McCulloch, A.D., 2001. Modelling cardiac mechanical properties in three dimensions. Philos. Trans. Roy. Soc. Lond. A 359, 1233–1250.

Janz, R.F., Kubert, B.R., Moriarty, T.F., 1974. Deformation of the diastolic left ventricle—II. Nonlinear geometric effects. J. Biomech. 7, 509–516.

Guccione, J.M., Costa, K.D., McCulloch, A.D., 1995. Finite element stress analysis of left ventricular mechanics in the beating dog heart. J. Biomech. 28, 1167–1177.

Hunter, P.J., Nash, M.P., Sands, G.B., 1997. Computational electromechanics of the heart. In: Panfilov, A.V., Holden, A.V. (Eds.), Computational Biology of the Heart. Wiley, West Sussex.

Hunter, P.J., McCulloch, A.D., ter Keurs, H.E.D.J., 1998. Modelling the mechanical properties of cardiac muscle. Prog. Biophys. Mol. Biol. 69, 289–331.

Hunter, P.J., Pullan, A.J., Smaill, B.H., 2003. Modelling total heart function. Annu. Rev. Biomed. Eng. 5, 147–177.

Keener, J.P., Sneyd, J., 1998. Mathematical Physiology. Springer, New York.

Makridakis, C.G., 1993. Finite element approximations of nonlinear elastic waves. Math. Comput. 61, 569–594.

Morton, K.W., Mayers, D.F., 1994. Numerical Solution of Partial Differential Equations. University Press, Cambridge.

Nash, M.P., Hunter, P.J., 2000. Computational mechanics of the heart. J. Elast. 61, 113–141.

Nash, M.P., Panfilov, A.V., 2004. Electromechanical model of excitable tissue to study reentrant cardiac arrhythmias. Prog. Biophys. Mol. Biol. 85, 501–522.

Nickerson, D.P., 2004. Modelling cardiac electro-mechanics: from cellML to the whole heart. PhD thesis, University of Auckland.

Nickerson, D.P., Smith, N.P., Hunter, P.J., 2005. New developments in a strongly coupled cardiac electromechanical model. Europace 7, S118–S127.

Niederer, S.A., Hunter, P.J., Smith, N.P., 2006. A quantitative analysis of cardiac myocyte relaxation: a simulation study. Biophys. J. 90, 1697–1722.

Noble, D., Varghese, A., Kohl, P., Noble, P.J., 1998. Improved guinea-pig ventricular cell model incorporating a diadic space, I_{Kr} and I_{Ks}, and length- and tension-dependent processes. Can. J. Cardiol. 14, 123–134.

Remme, E.W., Nash, M.P., Hunter, P.J., 2005 Distributions of myocyte stretch, stress and work in models of normal and infarcted ventricles. In: Kohl, P., Sachs, F., Franz, M.R. (Eds.), Cardiac Mechano-Electric Feedback and Arrhythmias: From Pipette to Patient. Saunders–Elsevier, UK.

Schneider, W., Bortfield, T., Schlegel, W., 2000. Correlation between CT numbers and tissue parameters needed for Monte Carlo simulations of clinical dose distributions. Phys. Med. Biol. 45, 459–478.

Simnett, S.J., Johns, E.C., Lipscomb, S., Mulligan, I.P., Ashley, C.C., 1998. Effect of pH, phosphate, and ADP on relaxation of myocardium after photolysis of diazo 2. Am. J. Physiol. Hear. Circ. Physiol. 275, 951–960.

Smith, N.P., Nickerson, D.P., Crampin, E.J., Hunter, P.J., 2004. Multiscale computational modelling of the heart. Acta Numer. 13, 371–431.

ten Tusscher, K.H.W.J., Noble, D., Noble, P.J., Panfilov, A.V., 2004. A model for human ventricular tissue. Am. J. Phys. Hear. Circ. Physiol. 286, 1573–1589.

Whiteley, J.P., 2006. An efficient technique for the solution of the monodomain and bidomain equations. IEEE Trans. Biomed. Eng. 53, 2139–2147.

Usyk, T.P., Mazhari, R., McCulloch, A.D., 2000. Effect of laminar orthotropic myofiber architecture on regional stress and strain in the canine left ventricle. J. Elast. 61, 143–164.